

Indian plate blocked by the thickened Eurasian crust in the middle of the continental collision zone of southern Tibet



Gaochun Wang^{a,b}, Xiaobo Tian^{a,c,*}, Yibing Li^{a,c}, Tao Xu^{a,c}, Bo Wan^{a,c}, Yi Chen^{a,c,**},
Shitan Nie^{a,c}, Xusong Yang^{a,c}, Sicheng Zuo^{a,c}, Jianli Zhang^{d,e}

^a State Key Laboratory of Lithospheric Evolution, Institute of Geology and Geophysics, Chinese Academy of Sciences, Beijing, 100029, China

^b Geothermal and Ecological Geology Research Center, School of Ecology and Environment, Zhengzhou University, Zhengzhou, 450001, China

^c Innovation Academy for Earth Science, CAS, Beijing, 100029, China

^d Frontiers Science Center for Deep Ocean Multispheres and Earth System, Institute for Advanced Ocean Study, Ocean University of China, Qingdao, 266100, China

^e Laboratory for Marine Mineral Resources, Pilot National Laboratory for Marine Science and Technology (Qingdao), Qingdao, 266237, China

ARTICLE INFO

Keywords:

Qinghai-Tibetan Plateau
Indian lithospheric slab
Wide-angle reflection/refraction
Crustal P-wave velocity structure
Crustal thickening

ABSTRACT

The relationship of the crustal contact between the Indian and Eurasian plates is a key issue in understanding crustal thickening and the subduction of the Indian lithosphere beneath the Qinghai-Tibetan Plateau. Across the middle of the Yarlung-Zangbo Suture (YZS), we deployed an ~450-km-long SN-trending wide-angle reflection/refraction profile to observe the P-wave velocity (v_p) structure beneath the northern Himalaya and the southern plateau. Our results show that, 1. the high v_p (~7.1 km/s) indicates that the Indian lower crust extends no more than 50 km north of the YZS. 2. The lower crust beneath the southern part of the plateau features an extremely low v_p ($<6.7 \pm 0.2$ km/s). 3. Compared with the velocities of several typical crustal lithologies in different temperature regimes, the low v_p in the lower crust can be explained by felsic-intermediate granulite, which has prevented the lower crust from further eclogitization. We propose that the dip angle of the Indian lithospheric slab beneath the YZS is partly controlled by the composition of the lower crust of the plateau. In the northern middle YZS, the crust of the southern plateau is too thick and blocks the northward advancement of the Indian lower crust, resulting in the subduction of the Indian lithospheric slab into the upper mantle. The lower crust in western and eastern Lhasa is dominated by a mafic composition, and it was delaminated after eclogitization before the Miocene. The void zone generated by delamination favors the flattening and underthrusting of the Indian lower crust.

1. Introduction

The ongoing continental-continental collision between the Indian and Eurasian plates has produced the Qinghai-Tibetan Plateau since the Cenozoic (Yin and Harrison, 2000). The Qinghai-Tibetan Plateau, the largest plateau on Earth today, is supported by an extremely thick crust, especially in the southern Qinghai-Tibetan Plateau, where the crustal thickness reaches ~80 km, which is twice that of the normal continental crust (Owens and Zandt, 1997; Zhang et al., 2011). How this thick crust

has formed and been preserved has been debated over the past several decades.

Eurasian crustal compression and shortening (Allégre et al., 1984; Dewey and Burke, 1973; England and Houseman, 1986; Houseman and England, 1993) and mantle magmatic underplating derived by both the subducted Neo-Tethyan oceanic crust and the subducted Indian continental crust (Mo et al., 2007; Mo et al., 2008; Zhu et al., 2017) have been considered to play main roles in forming the thick crust beneath the Qinghai-Tibetan Plateau. Based on crustal structure images along several

* Corresponding author. State Key Laboratory of Lithospheric Evolution, Institute of Geology and Geophysics, Chinese Academy of Sciences, Beijing, 100029, China.

** Corresponding author. State Key Laboratory of Lithospheric Evolution, Institute of Geology and Geophysics, Chinese Academy of Sciences, Beijing, 100029, China.
E-mail addresses: txb@mail.iggcas.ac.cn (X. Tian), chenyi@mail.iggcas.ac.cn (Y. Chen).



receiver function profiles, the flat underthrusting Indian lower crust has also been proposed to contribute to crustal thickening beneath the southern part of the plateau (Nábelek et al., 2009; Schulte-Pelkum et al., 2005; Shi et al., 2015; Wittlinger et al., 2009; Zhang et al., 2014). The changes in the subduction angle and northward horizontal stretching distance of the Indian continental slab in the east-west direction (Li et al., 2008; Zhao et al., 2010), however, suggest spatially varying contact relationships between the Indian crust and the Eurasian crust along the collision zone.

Studies of whole-rock or mineral geochemical signatures (Zhu et al., 2017) indicate that the crustal thickness beneath the southern Qinghai-Tibetan Plateau reached ~70 km at approximately 20–10 Ma. Lower crustal mafic rocks can transfer to eclogite facies at depths exceeding 50 km [O'Brien and Rötzler, 2003]. High-density eclogites, which are denser than mantle peridotites, become potentially gravitationally unstable to founder into the deep mantle (Lee and Anderson, 2015). In this case, it is almost impossible to increase the crustal thickness to 80 km, and the extremely thick crust beneath the Qinghai-Tibetan Plateau is therefore unstable and short-lived. Petrologic observations and experimental studies have indicated that eclogitization is not only controlled by pressure and temperature conditions but also influenced by whole-rock composition (De Paoli et al., 2012; Green and Ringwood,

1972). The composition of crustal rocks (especially the lower crust) remains largely speculative in Tibet due to the rarity of xenoliths and exhumed lower crustal granulites, which are direct evidence for constraining the composition of the lower crust (Chan et al., 2009; Kang et al., 2020).

The seismic P-wave velocity (v_p) is another way to constrain the petrological features of the crust (Christensen and Mooney, 1995). The wide-angle reflection and refraction (WARR) method is a recognized approach to obtaining the crustal P-wave velocity (v_p); however, the WARR profiles are sporadically distributed in the southern Qinghai-Tibetan Plateau (Fig. 1), which were deployed several decades ago before the advent of high-precision digital seismographs (Teng et al., 1983; Xiong and Liu, 1997; Zhang et al., 2011; Zhang and Klempner, 2010; Zhang and Klempner, 2005), resulting in insufficient constraints on the crustal v_p , especially the lower crust of the plateau.

In the middle of the continental collision zone, southern Lhasa has the thickest crust on the plateau (Zhang et al., 2011), and the Himalayan orogen features the most intense crustal deformation, as indicated by Mount Everest and HP-UHP rocks (Guillot et al., 2008; Lombardo and Rolfo, 2000; Zhang et al., 2015). Therefore, we deployed a WARR profile from the Bangong-Nujiang suture (BNS) to the Tethyan Himalaya (TH) along 88.5°E longitude to investigate the velocity structure of the whole

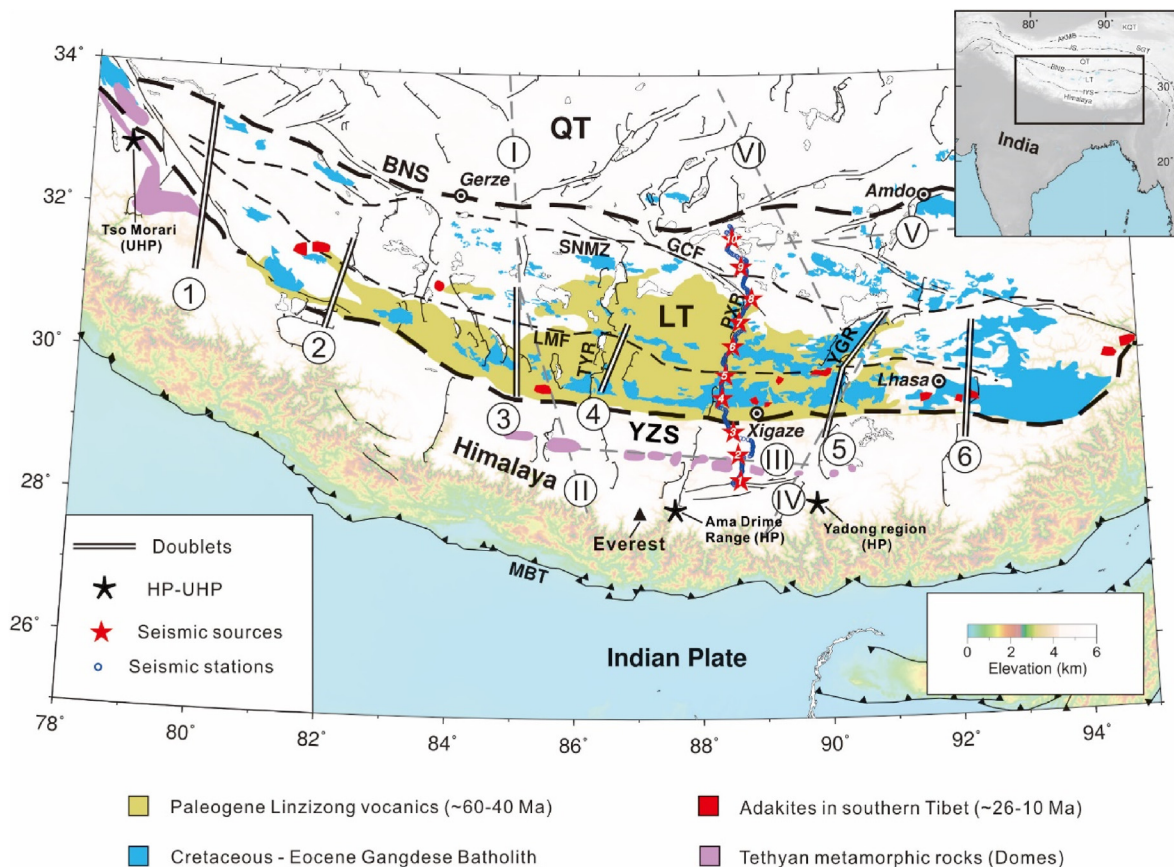


Fig. 1. Geological map of the southern Qinghai-Tibetan Plateau and the location of the wide-angle reflection and refraction (WARR) profiles. Blue circles show the stations along the seismic profile, and red stars with numbers mark the shots. The geological map is compiled by Kapp et al. (2005), Wang et al. (2013), and Zhang et al. (2010). The faults are modified from Taylor and Yin (2009), Zhu et al. (2011), and Hou et al. (2015). The distributions of adakite rocks are compiled from Chung et al. (2003) and Guo et al. (2013). The black stars show the locations of the high-to ultrahigh-pressure metamorphic rocks (Guillot et al., 2008; Zhang et al., 2015). Double railway lines denote receiver function doublets marked by the numbers in the circles. 1: Zhang et al. (2014), 2: Xu et al. (2017), 3: Nábelek et al. (2009), 4: Xu et al. (2015), 5: Kind et al. (2002), 6: Shi et al. (2015). The previous wide-angle reflection/refraction profiles (marked by the Roman numerals in the circles) are also included; I: Xiong and Liu (1997), II: Liu (2003), III: Zhang and Klempner (2010), IV: Teng et al. (1983), V: Zhang and Klempner (2005), VI: Zhao et al. (2001). In the inset map, the black rectangle denotes the study area. AKMS = Aiyimaqin-Kunlun-Muztagh suture; JS = Jinsha suture; BNS = Bangong-Nujiang suture; YZS = Yarlung-Zangbo suture; KQT = Kunlun-Qilian terrane; SGT = Songpan-Ganze terrane; QT = Qiangtang terrane; LT = Lhasa terrane; SNMZ = Shiquan River-Nam Tso Mélange Zone; LMF = Luobadui-Milashan Fault; PXR = Pengqu-Xianzha rift; TYR = Tangra YumCo rift; MBT = Main Boundary Thrust; GCF = Gyaring Co Fault; HP-UHP = high-to ultrahigh-pressure metamorphic rocks.

crust. We used the high-resolution crustal v_p to constrain the deep crustal composition as well as the relationship between the crust beneath the southern Qinghai-Tibetan Plateau and the northward advancing Indian lithosphere.

2. Tectonic setting

The Qinghai-Tibetan Plateau (Fig. 1) is formed by the amalgamation of several terranes (Allégre et al., 1984; Chang et al., 1986; Yin and Harrison, 2000), from north to south, including the Kunlun-Qilian terrane (KQT), the Songpan-Ganze terrane (SGT), the Qiangtang terrane (QT), the Lhasa terrane (LT) and the Himalaya, which are separated by the Ayimaqin-Kunlun-Muztagh suture (AKMS), Jinsha suture (JS) and Bangong-Nujiang suture (BNS), respectively. The Yarlung-Zangbo Suture (YZS) is recognized as the collision boundary between the Indian and Eurasian plates separating the Lhasa terrane and the Himalayas. The Qinghai-Tibetan Plateau is underlain by a thick crust with an average elevation of ~ 4000 m. Based on broadband seismic arrays in the plateau, receiver function studies have shown that the average crustal thickness is approximately 65 km, and the crustal thickness is largest (more than 80 km) in the southern Lhasa terrane and decreases northward to less than 65 km beneath the BNS. Beneath the Himalayas, the crust thickens from 40 km in the northernmost Indian plate to 70–80 km under the YZS (Kind et al., 2002; Mitra et al., 2005; Nábelek et al., 2009; Schulte-Pelkum et al., 2005; Shi et al., 2016; Wittlinger et al., 2009; Xu et al., 2017; Yuan et al., 1997; Zhang et al., 2014).

Receiver function images show a continuous positive phase 15 km above the Moho, which has been interpreted as the top of the Indian lower crust intruding into the plateau crust (Nábelek et al., 2009). Almost all studies of N-S-trending broadband arrays across the western or eastern part of the YZS (Fig. 1) suggest that the Indian lower crust presents as a ~ 150 -km-long flat-lying layer on the bottom of the Lhasa crust (Kind et al., 2002; Nábelek et al., 2009; Shi et al., 2016; Xu et al., 2015, 2017; Zhang et al., 2014). Based on seismic reflection images, however, Guo et al. (2017) proposed that the Indian lower crust, accompanied by mantle lithosphere, subducts into the upper mantle beneath the middle of the YZS with a north-dipping angle of ~ 27 – 45° . Local earthquake tomography revealed a high v_p (> 7.0 km/s) in a depth range from 50 to 70 km, which explains the partial eclogitization of the Indian lower crust beneath the Himalayas (Monsalve et al., 2008). Studies of a W-E-trending WARR profile in the Himalaya, however, obtained a v_p of the Indian lower crust of less than 7.0 km/s (Teng et al., 1983; Zhang et al., 2004). Unlike the eclogitized Indian lower crust ($v_p > 7.3$ km/s) (Wittlinger et al., 2009) interpreted by receiver function results, two N-S-trending WARR profiles crossing the YZS showed that the v_p is less than 7.0 km/s in the lower crust beneath the southern Lhasa terrane (Liu, 2003; Teng et al., 1983). In the northern Lhasa terrane, a slightly high v_p (6.9–7.2 km/s) in the lower crust was detected under a W-E-trending WARR profile (Zhang and Klemperer, 2005). Along the INDEPTH-III profile, WARR results showed that the v_p of the lower crust increases from 6.5 km/s at a depth of 47 km–7.3 km/s at a depth of 67 km (Zhao et al., 2001).

The Lhasa terrane can be divided into the northern, central, and southern Lhasa terrane (Hou et al., 2015; Zhu et al., 2011) based on differences in the sedimentary cover (Fig. 1). These three subterrane are separated by the Shiquan River-Nam Tso Mélange Zone (SNMZ) and Luobadui-Milashan Fault (LMF) (Zhu et al., 2011) from north to south (Fig. 1). The central Lhasa terrane has Proterozoic and Archean basement rocks based on Hf isotope anomaly results, but the southern and northern Lhasa terranes have Phanerozoic juvenile crust (Hou et al., 2015; Zhu et al., 2011). Petrogenetic studies show that the closure of the Neo-Tethyan Ocean and the Indo-Eurasian continental collision created widespread volcanic rocks and crustal thickening in the Lhasa terrane (Chung et al., 2005; Coulon et al., 1986; Harris et al., 1990; Molnar et al., 1993; Yin and Harrison, 2000; Zhu et al., 2009). The most prominent

magmatic events are the Cretaceous-Tertiary Gangdese batholith and the Linzizong volcanic succession (~ 65 – 40 Ma) (Allégre et al., 1984; Coulon et al., 1986; Murphy et al., 1997; Yin and Harrison, 2000). Recent petrological evidence suggests that upwelling mantle material and magmatic differentiation have a profound effect on crustal thickening (~ 15 – 20 km) in southern Tibet based on abundant magmatism, including large-scale cotemporaneous felsic magmatic rocks (~ 70 – 45 Ma) in the Gangdese magmatic belt and widespread Linzizong volcanic succession (~ 65 – 40 Ma) (Mo et al., 2007; Mo et al., 2008; Zhu et al., 2017).

3. Seismic data and methods

We carried out a 450-km-long south-north WARR profile from the Himalayas through the YZS to the BNS along approximately 88.5°E (Fig. 1) from September to October 2016. Because of the extremely harsh environment, seismic stations were deployed along the only road near the Pengqu-Xianzha rift (PXR) from Gangba to Selin Co Lake. The profile was composed of 311 digital seismic stations equipped with 2.5-Hz-short period 3-D component geophones, with a spacing of 1.3 km and sampling of 100 Hz. Seismic signals were produced by 10 shots with an interval of ~ 45 km, including four large shots (4 t of dynamite) at the two ends of the profile (shot 01, shot 02, shot 09 and shot 10) and six shots with 2 t of dynamite (shots 03–08). The shot parameters are shown in Table S1. Each shot was triggered in a borehole pattern at a depth of ~ 50 m. The clock in the seismic instrument was set by a GPS time service system 1–12 hr before each shotting. As a result, ~ 0.025 s of time bias could be introduced into our data by an automatic crystal oscillator. We obtained 5-minute-long records at all 311 seismic stations for each shot. Some station records were noisy due to strong winds and are rejected in further studies. Shot 02 with 4 t of dynamite only produced records with a small offset by failure blasting.

In the WARR method, data processing generally consists of three steps, including data preprocessing, seismic phase identification, and velocity structure inversion. During preprocessing, the raw seismic data were reduced by 6.0–8.0 km/s. Seismic phases from the crust and upper mantle were identified, and travel times were picked by using the *splot* (Piotr Środa modified the *splot* of C. A. Zelt) (Zelt and Smith, 1992) software package after filtering the data at 2–10 Hz. The 2-dimensional P-wave velocity structure of the shallow crust was calculated by the finite difference method (Hole, 1992; Vidale, 1988) using the first arrivals of the diving wave in the sediment and the crystalline upper crust in all seismic sections. Then, we used the software packages FAST (Zelt and Barton, 1998) and RAYINVR (Zelt and Smith, 1992) to construct the whole crust and uppermost mantle velocity structure. Velocity modeling was performed following the “across and down” approach (Zelt and Smith, 1992) in which the early seismic phase was fitted to obtain a shallow structure, which was used as the input model for the deep structure to fit the late seismic phase. After data preprocessing, the first arrivals (the P_g phases refracted from the sedimentary cover and the crystalline basement) can be traced to more than 100 km in almost all shots (Fig. 2, S1 and S2, and Table 1). The later arrivals are characterized by a relatively low signal-to-noise ratio (SNR) due to the thick crust in the south-central Qinghai-Tibetan Plateau (Liu, 2003; Owens and Zandt, 1997; Zhang et al., 2011). There are several rules for picking seismic reflection phases in the crust. First, the theoretical time-distance curve of the reflection arrivals of the horizontal interface is hyperbolic. Based on this principle, we picked arrivals with a high signal-to-noise ratio first. Second, these traces with relatively low signal-to-noise ratios were filtered by different frequency ranges to improve the SNR, and then we picked the arrivals reflected on the interface traced by high SNR arrivals. Third, the point at which frequency changed along one trace was also used to recognize the arrival near the hyperbolic time-distance curves. Finally, the reciprocity arrivals were used to improve the precision of the picks. Following the approaches mentioned above, the seismic reflection phases, including the arrival times of the P waves reflected from the crustal discontinuities ($P_{c1}P$, $P_{c2}P$, $P_{c3}P$, $P_{c4}P$ and $P_{c5}P$) and arrivals

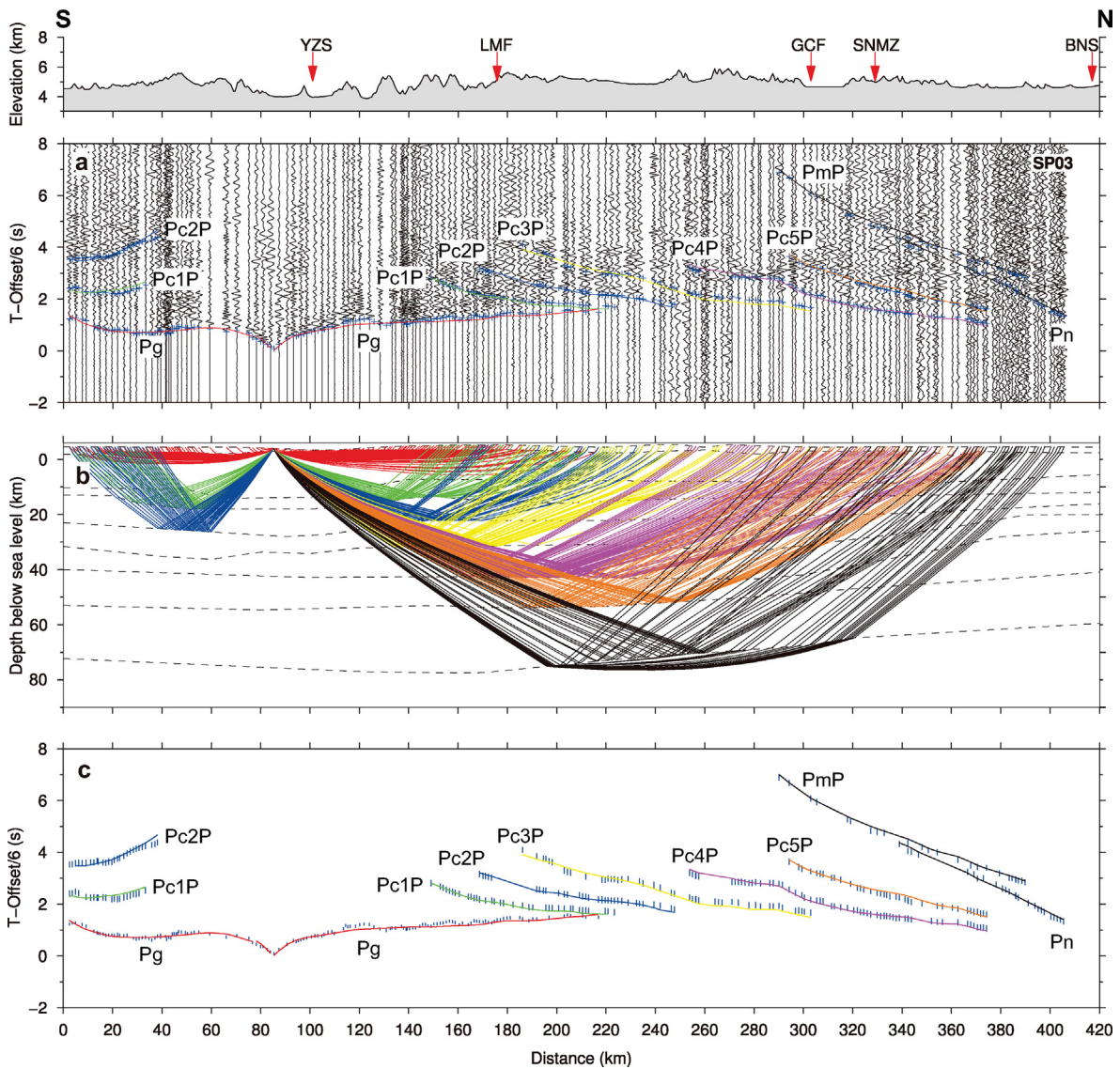


Fig. 2. Seismic sections of shot 03 with phase picks, ray tracing and travel time fitting results. The travel time is reduced by a velocity of 6.0 km/s. The uppermost slice shows the elevations and locations of the main faults along the seismic profile. (a) Seismic section with picks (blue crosses) and the calculated times (colored lines). (b) Ray paths are calculated from the final velocity model in the shot 03 section. The rays of different phases are distinguished by the same colors as those in (a). (c) Picks (blue bars) and calculated times (colored lines); the length of the bars denotes the uncertainty of the picks.

reflected from the Moho discontinuity (P_mP), were chosen individually (Fig. 2 and S2-3, and Table 1). To obtain a more credible v_p velocity model picks with large uncertainties were rejected in this study. As a result, 3 337 picks were chosen, which is less than the 3 665 picks in the previous study of this profile by Wang et al. (2021). For the reflections, we assumed that all the reflections are supercritical reflections. The apparent velocity at the beginning distance (the critical point) of the reflections represents the velocity beneath the interface, and the apparent velocity at the far end of the reflections is the maximum velocity above the interface (Table 1). The influence of the dipping interface on the velocities could be corrected from ray tracing and arrival time inversion. Diving waves, P_n (refractions from the uppermost mantle), were used to invert the uppermost mantle velocity directly.

V_1^* is the apparent velocities at the beginning distance (the critical point) of the reflections which represents the velocity beneath the interface. V_2^* is the apparent velocity at the far end of the reflections is the maximum velocity above the interface.

4. Results

4.1. Model reliability analysis

Approximately 99.5% of the arrival times were used to calculate the 2-D velocity structure (Table S2). The calculated arrivals of all phases fit the real seismic data well (Fig. S4c, Table S2). The ray coverage of the Moho and upper mantle show that they can constrain the central profile between 110 km and 330 km distances well (Fig. S4b). An uncertainty of 150 ms is associated with all arrival time picks. The root mean square (RMS) of the travel time residuals (t_{RMS}) between the modeling and observations are less than 110 ms for each shot (Table S2). The smaller the chi-squared value is, the closer the calculated model is to the true model (Zelt and Smith, 1992). A $\chi^2 < 1.65$ is achieved for every shot (Table S2), except for the noneffective propagation of shot 02. For every seismic phase, a $\chi^2 < 2.59$ is acquired (Table S2). We use the diagonal values of the resolution matrix to measure the model reliability for

Table 1
Description of seismic phases.

Phase	Layer	Depth (km)	V1* (km/s)	V2* (km/s)	Observation distance (km)
Pg	—	0-21	—	5.6–6.3	SP01: 0-160; SP02: 0-100; SP03: 0-220; SP04: 0-250; SP05: 60-280; SP06: 100-310; SP07: 170-350; SP08: 210-400; SP09: 230-410; SP10: 270-410.
Pc1P	C1	15-21	6.2–6.4	6.2–6.3	SP01: 30-160; SP03: 0-40 and 140-220; SP04: 10-60 and 160-270; SP05: 30-80 and 230-310; SP06: 80-160 and 290-370; SP07: 150-220 and 310-380; SP08: 140-240 and 320-390; SP09: 220-290 and 280-410; SP10: 270-340.
Pc2P	C2	22-33	6.4–6.5	5.8–6.4	SP01: 80-200; SP03: 0-40 and 160-240; SP04: 30-50 and 200-300; SP05: 0-60 and 230-360; SP06: 60-140 and 290-380; SP07: 130-210 and 300-410; SP08: 130-220 and 340-410; SP09: 150-270 and 380-410; SP10: 250-330.
Pc3P	C3	27-42	6.6–6.7	6.4–6.5	SP01: 80-210; SP03: 180-310; SP04: 250-370; SP05: 10-60 and 290-400; SP06: 50-140 and 360-410; SP07: 110-190 and 330-410; SP08: 80-180 and 360-410; SP09: 140-230 and 380-410; SP10: 160-310.
Pc4P	C4	33-48	6.7–7.0	6.5–6.6	SP01: 160-220; SP03: 250-370; SP04: 290-410; SP05: 330-410; SP06: 20-70 and 370-410; SP07: 5-90 and 330-410; SP08: 70-140 and 380-410; SP09: 140-180; SP10: 130-210.
Pc5P	C5	47-59	—	6.6–6.7	SP01: 160-260; SP03: 290-370; SP04: 300-410; SP05: 330-410; SP06: 10-50 and 370-410; SP08: 60-100 and 380-410; SP09: 140-180; SP10: 100-220.
PmP	Moho	64-84	—	6.7–6.8	SP01: 250-410; SP03: 280-400; SP04: 370-410; SP05: 370-410; SP08: 0-90; SP09: 0-110; SP10: 10-90.
Pn	—	—	—	7.6–8.1	SP01: 270-400; SP03: 340-410; SP08: 0-60; SP09: 10-90; SP10: 0-90.

depths and velocities (Zelt, 1999; Zelt and Smith, 1992). Both the velocity and depth perturbations are inverted at both depth and velocity nodes. Resolution tests (Fig. S5) show that all velocity nodes and the depth nodes are well resolved in the areas with good ray coverage.

4.2. Velocity model

The shallow crustal velocity structure is shown in Fig. 3c. A velocity contour of 5.6 km/s is used to represent the top of the crystalline basement. In the southern YZS, a low-velocity anomaly that thickens northward is associated with thick sediments in the suture. And there are ~0.8–1.0 s delay for the travel time of P_g as shown in the reduced seismic sections of SP04, SP05, and SP06. The thickness of the sedimentary succession is approximately 3.5 km in the central Lhasa terrane with velocities between 3.3 and 5.6 km/s, and the same thickness of sedimentary cover can also be observed at the north end of the profile near Selin Tso with velocities between 3.6 and 5.6 km/s. In the southern Lhasa terrane from 120 to 170 km in the profile, the high-velocity zone underlying a thin sedimentary layer agrees with the Gangdese magmatic

belt, which developed by extensive granitoid intrusions in a Cretaceous-early Cenozoic Andean-type arc (Schärer et al., 1984; Yin and Harrison, 2000). The v_p structure changes abruptly near the Gyaring Co fault (GCF), from approximately 4.0–5.6 km/s in the south to 5.4–6.0 km/s in the north. This results in ~0.6 s of P_g travel time delay in the SP07 and SP08 reduced seismic sections near the ~300 km distance.

The whole crustal velocity structure is illustrated in Fig. 3d. The P-wave velocity rapidly increases to ~6.3 km/s from the bottom of the sedimentary crust to the crystalline crust. The vertical velocity gradient is homogeneous from the top crystalline crust to a depth of ~15 km (0 km depth represents sea level) in the Lhasa terrane, with velocities varying from 5.8 to 6.3 km/s. In the Tethyan Himalaya, however, a high-velocity anomaly (6.1–6.4 km/s) is observed just below a 2-km-thick sedimentary cover down to a depth of ~20 km at a distance ranging from 20 km to 100 km, which represents the North Himalayan gneiss dome. In the Lhasa crust, a low-velocity zone (LVZ) with a thickness of approximately 6–8 km is present at a depth of 10–20 km between 230 km and 340 km. The velocity of the LVZ is approximately 6.0–6.2 km/s with a 2.1–6.2% velocity decrease relative to the velocity of the upper layer. From a depth of 10–40 km, the velocity is 6.4–6.8 km/s in the Himalayan terrane (60 km–100 km distance) and becomes lower than 6.6 km/s in the south Lhasa terrane and lower than 6.5 km/s in central Lhasa, and then increases to 6.6 km/s north of the GCF. In the lower crust, the Indian plate has a normal velocity value of 7.0–7.2 km/s, which corresponds with previous studies (Monsalve et al., 2008; Sheehan et al., 2014; Vijaya Rao et al., 2015). The velocity is approximately 6.8 km/s in the lower crust of the southern Lhasa terrane. However, an extremely low velocity (≤6.7 km/s) is observed beneath the central-northern Lhasa terrane. The P_n velocity (the v_p in the uppermost upper mantle) is approximately 8.1 km/s in the distance range of 110–250 km and then decreases to ~7.6 km/s in the distance range of 250–320 km.

The whole crustal average velocity is 6.38 km/s (Fig. 3f). The average crustal velocity in the Tethyan Himalaya (6.47 km/s) is higher than that in the Lhasa terrane. The central Lhasa terrane has an extremely low average crustal velocity (6.32 km/s). Beneath the YZS, the Moho discontinuity deepens from ~75 km beneath the Tethyan Himalaya to 79 km beneath the Lhasa terrane. Then, the depth of the Moho discontinuity decreases northward from ~75 to 79 km in the southern Lhasa terrane, to ~75 km in the central Lhasa terrane and ~65–70 km in the northern Lhasa terrane.

5. Discussion

5.1. Crustal structure in the Himalayas and southern Tibet

Several transmeridional faults are observed in the shallow velocity structure in the Lhasa terrane (Fig. 3b and c). For example, the positions of the LMF and SNMZ inferred from geological observations (Hou et al., 2015; Zhu et al., 2011) are also marked by high-velocity anomalies (Fig. 3c). According to the shallow velocity structure, we divide the Lhasa terrane into the southern Lhasa terrane, the central Lhasa terrane, and the northern Lhasa terrane from south to north, respectively. According to the velocity model, the top of the crystalline basement is ~3 km below the surface. In the results, the relatively homogeneous velocity of ~6.4 km/s in the upper crust (10–30 km) beneath the Lhasa terrane provides seismic evidence of a lack of tectonic deformation. The essentially flat-lying Gangdese batholith and the Linzizong volcanic rocks (late Paleocene-early Eocene ~65–40 Ma volcanic sequence), which are well exposed in the southern Lhasa terrane, also imply that there has been no significant north-south shortening in the upper crust since the Cenozoic in the Lhasa terrane (Coulon et al., 1986; Murphy et al., 1997; Yin and Harrison, 2000).

Beneath the Himalaya and YZS, the results show a north-dipping velocity changing boundary at a depth range of 30–80 km and a distance range of 70–160 km (Fig. 3d and e), which separates a high-v_p (~7.20 ± 0.2 km/s) lower crust to the south and a low-v_p (6.7–6.9 km/s)

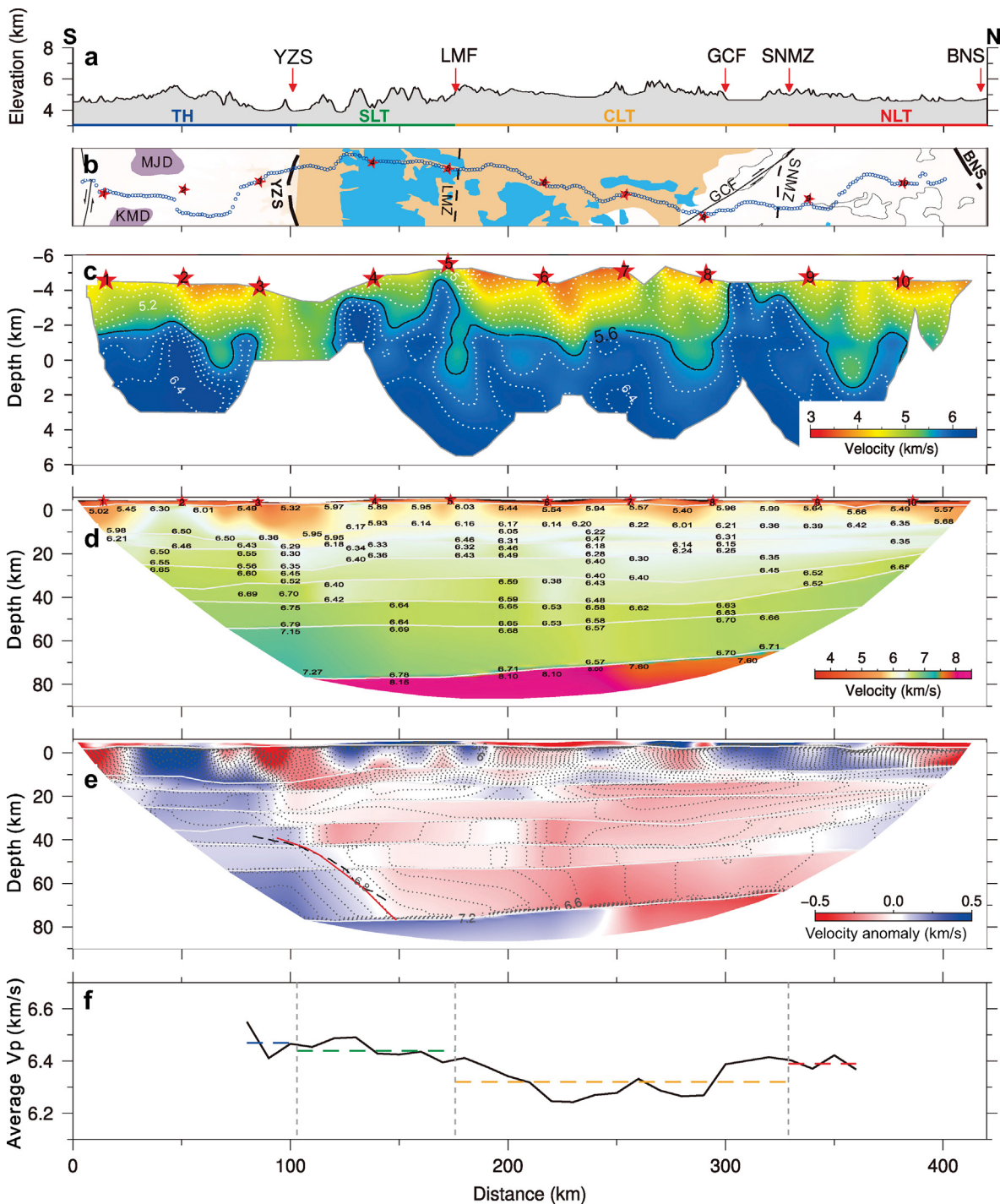


Fig. 3. The final velocity model. (a) Topography and location of the main faults along the seismic profile. (b) Geological map along the seismic profile in this study. Blue circles show the stations along the seismic profile in this study, and red stars with numbers mark the seismic sources. (c) Shallow crustal v_p structure calculated by the finite difference method (Hole, 1992; Vidale, 1988) using the first arrivals (P_g phase). The isoline of 5.6 km/s marked by the solid line represents the top of the crystalline crust. (d) Whole crustal v_p structure is calculated by the software RAYINVZ (Zelt and Smith, 1992). Discontinuities are marked by white lines. (e) The velocity anomalies Δv_p are plotted with the contour lines of the v_p . Δv_p is calculated by the v_p minus the average v_p of the same depth. Beneath the v_p , the red line denotes the Main Himalayan Thrust (MHT) revealed by our velocity model, while the blue dashed line shows the MHT from Guo et al. (2017). (f) Crustal average P-wave velocity calculated from our velocity model. MJD = Mabja Dome; KMD = Kampa Dome; TH = Tethyan Himalaya; SLT = Southern Lhasa Terrane; CLT = Central Lhasa Terrane; NLT = Northern Lhasa Terrane.

lower crust to the north with a north-dipping angle of $\sim 35^\circ$. Previous seismic tomography (Monsalve et al., 2008; Vijaya Rao et al., 2015) has shown that the Indian lower crust features a high v_p (>7.0 km/s). We interpret the north-dipping boundary beneath the northern Himalayas and YZS as the top of the subducted Indian lower crust, with a similar

position as the main Himalayan thrust (MHT) proposed by previous studies (Fig. 4b) (Guo et al., 2017; Li et al., 2018; Murphy, 2007). The results of this study suggest that the northward advancing Indian lower crust terminates in the southernmost Lhasa terrane, which is supported by the deep seismic reflection results and the magnetotelluric results

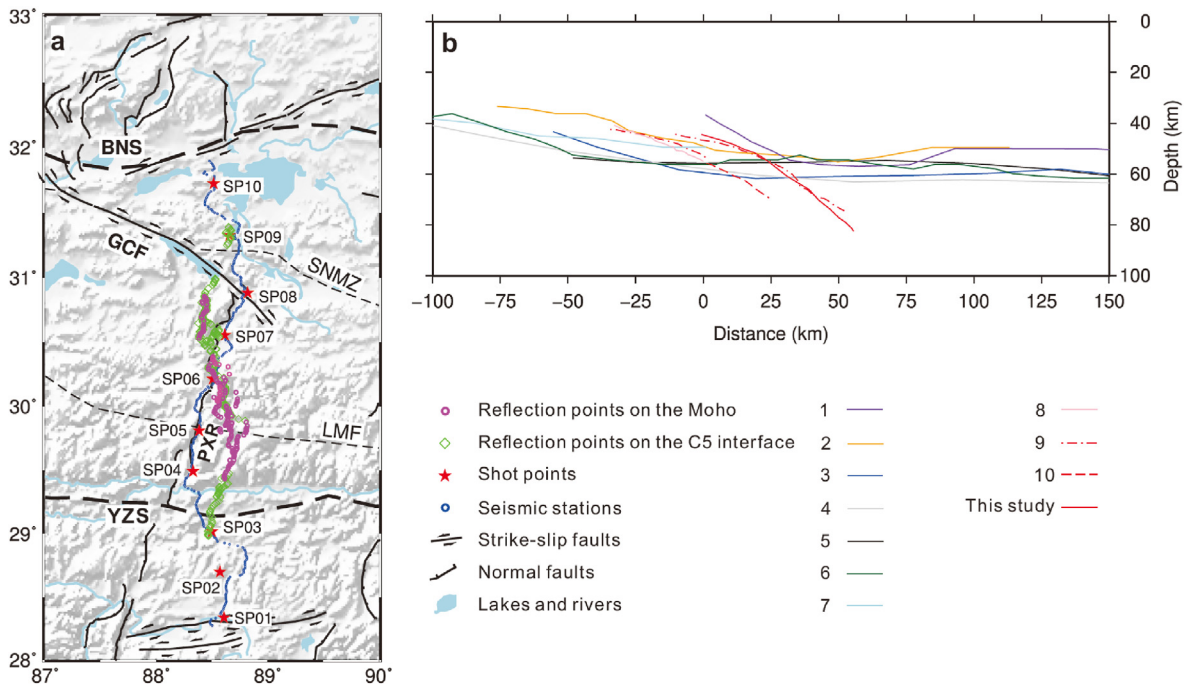


Fig. 4. (a) The distribution of reflection points at the C5 interface (green circles) and Moho discontinuity (purple circles). Blue circles and red stars show the stations and the shots. (b) Geometric morphology of the MHT or the top of the Indian lower crust. The zero km distance denotes the location of the Yarlung-Zangbo suture (YZS). The red lines show the results of the observations in N-S geophysical profiles in the middle part of the southern Qinghai-Tibetan Plateau. The other colored lines show the receiver function results from the N-S profiles in the western and eastern Qinghai-Tibetan Plateau. 1: Zhang et al. (2014), 2: Xu et al. (2017), 3: Nábelek et al. (2009), 4: Xu et al. (2015), 5: Kind et al. (2002), 6: Shi et al. (2015), 7: Schulte-Pelkum et al. (2005), 8: Murphy (2007), 9: Guo et al. (2017), 10: Li et al. (2018).

(Guo et al., 2017; Liang et al., 2018). The results show that the P-wave velocity is less than 6.7 km/s in the lower crust of the Lhasa terrane. The seismic observations deviate obviously from the mafic lower crust, which is characterized by a v_p that is larger than 6.8 km/s (Christensen and Mooney, 1995; Rudnick and Fountain, 1995; Rudnick, 1995; Rudnick and Gao, 2003).

5.2. The low v_p layer at the bottom of the upper crust

A low-velocity layer (LVL), with a decrease in velocity of ~ 0.1 – 0.3 km/s, is observed at the bottom of the upper crust (in a depth range of 17–25 km) at a distance of ~ 230 – 340 km in the central Lhasa terrane. The LVL in the deep middle or lower crust has been taken as an important indicator of a low-viscosity crustal channel for the channel flow model, in which crustal material migrates from the center to the edge of the plateau induced by gravitational potential energy (Beaumont et al., 2001; Clark and Royden, 2000; Royden et al., 2008). It has been debated for decades whether channel flow exists and controls the topographic evolution in the Qinghai-Tibetan Plateau, although low shear wave velocity zone in the middle crust at depths of ~ 20 – 40 km (e.g., Huang et al., 2020; Liu et al., 2014; Yang et al., 2012), high-conductivity layers in the middle crust (e.g., Li et al., 2003; Liang et al., 2018; Unsworth et al., 2005; Wei et al., 2010), and the low- Q_{lg} belt indicate high seismic wave attenuation (Zhao et al., 2013) are frequently observed in the plateau and its margin.

For the crustal high-conductivity layer in southern Tibet, magnetotelluric analysis suggests that the melting fraction of crustal rocks can reach 5%–14%, but it is not enough to weaken the rock-to-flow conditions for granite (Wei et al., 2010). Li et al. (2003) explained the high-conductivity anomaly by saline fluids because middle-lower crustal partial melting and a thin layer of water in the shallow crust can produce the same MT data. Both partial melting and fluid water can decrease seismic velocities (Watanabe, 1993), but the v_p/v_s ratio is a good parameter to distinguish partial melting and fluid water in rocks. For partial melting in rocks, the v_p/v_s ratio increases with increasing melting fraction; however, it decreases with increasing fluid fraction for rocks

with saline fluid water (Watanabe, 1993). Normal-to-low crustal average v_p/v_s ratios (Owens and Zandt, 1997; Wittlinger et al., 2009) suggest a lack of partial melting in the southern and central Lhasa terrane. Here, we suggest that the LVZ is caused by a thin layer (~ 6 – 8 km) with saline fluid water at the bottom of the central Lhasa upper crust, although it has not been found in the WARR model along the INDEPTH-III profile (Haines et al., 2003; Zhao et al., 2001).

5.3. The lower crustal composition beneath the southern plateau

We extracted typical crustal velocity profiles from different crustal lithologies and compared them to typical velocity versus depth curves in the Tethyan Himalaya and southern, central, and northern Lhasa terranes (Fig. 5). Four kinds of lower crustal compositions are chosen as candidates, including granite gneiss (GGN), felsic granulite (FGN), intermediate granulite (IGR) and mafic granulite (MGR) (Christensen, 1979; Christensen and Mooney, 1995). According to the calculation, the v_p resulting from mafic granulite at lower or average temperatures best fits the observations in the Tethyan Himalaya (Fig. 5a and b). The felsic and intermediate granulites under both lower and normal geothermal conditions (Fig. 5a and b) can result in a low v_p , which matches the observation velocity in the lower crust of the Lhasa terrane well. Under high geothermal conditions (Fig. 5c), the temperature increases from 800 °C at a depth of 60 km–1000 °C at a depth of 80 km, and the v_p decreases in the mafic granulite when compared with the values at low (Fig. 5a) and normal (Fig. 5b) temperatures, but the v_p values of 6.9 km/s are still higher than the low v_p (6.7 km/s) beneath the southern Qinghai-Tibetan Plateau. Partial melting in the lower crust is another factor that decreases the v_p , but it is opposed by geophysical observations. First, a new three-dimensional crustal conductivity structure (Dong et al., 2020) shows no highly conductive lower crustal anomalies deeper than 65 km in the central and southern Qinghai-Tibetan Plateau. Second, if the low v_p in the depth range from 60 km to 80 km is induced by partial melting, the crustal average v_p/v_s ratios should increase pervasively in the southern Qinghai-Tibetan Plateau; however, conversion wave analysis (Nábelek

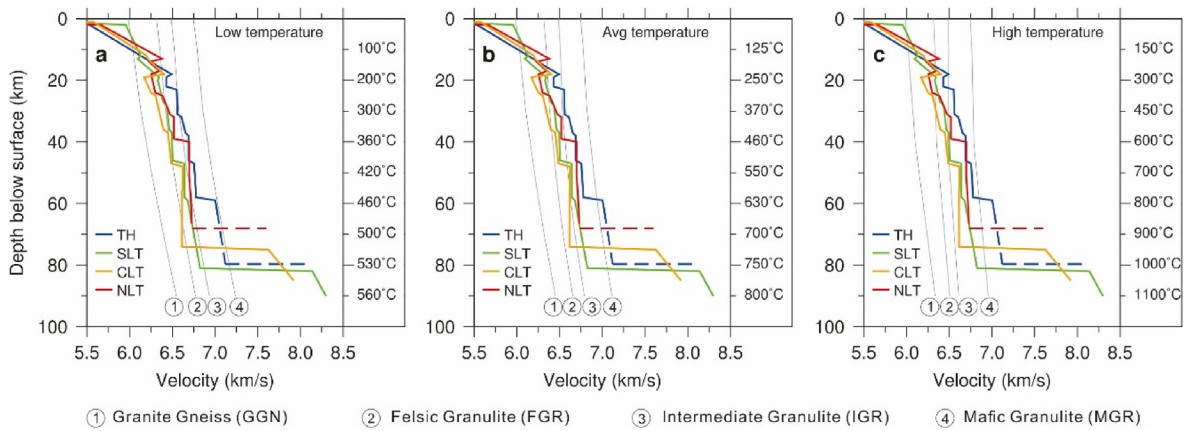


Fig. 5. Comparison of velocity structures between the results of the WARR profile in this study (colored lines) and several major rock types (gray lines). (a), (b), and (c) show the comparison at low, average, and high-temperature conditions, respectively. Based on the measurements $V(z_0)$ in the laboratory under surface conditions (Christensen and Mooney, 1995), as well as pressure gradients (dV/dP) and temperature gradients (dV/dT) (Christensen, 1979), the velocity value at a depth of z is calculated by $V(z) = V(z_0) + \frac{dV}{dP} \cdot \frac{dP}{dz} \cdot (z - z_0) + \frac{dV}{dT} \cdot \frac{dT}{dz} \cdot (z - z_0)$, where P is the pressure and T is the temperature. Amphibolite (AMP) is also considered to have velocities close to those of mafic granulite rocks. TH: Tethyan Himalaya; SLT: Southern Lhasa terrane; CLT: Central Lhasa terrane; NLT: Northern Lhasa terrane.

et al., 2009; Owens and Zandt, 1997) shows a low crustal average v_p/v_s ratio in the Lhasa terrane. In this study, seismometers of the WARR profile were placed along the PXR. Several previous studies suggest that these N-S-trending rifts in southern Tibet extend from the surface to the Moho depth (Guo et al., 2018; Tian et al., 2015; Wang et al., 2017). The reflection points in the lower crust (green rhombus at the C5 layer and purple circles at the Moho in Fig. 4a) show that only a small fraction of these rays partly travel along or through the PXR unless the rift becomes wider in the deep crust. The magnetotelluric profile along the PXR (Liang et al., 2018) shows a normal-conductivity lower crust beneath the central and northern Lhasa terrane, which rules out the low v_p caused by partial melting. Based on the above analysis, we employ the felsic-intermediate granulite to explain the extremely low v_p in the lower crust beneath the central and northern Lhasa terrane.

5.4. Comparison with previous receiver function studies

Previous receiver function results have imaged a ~ 15 -km-thick high- v_s layer (bounded by a doublet) in the lower crust beneath the southern Qinghai-Tibetan Plateau, which was interpreted as the underthrust of the Indian lower crust (Kind et al., 2002; Nábelek et al., 2009; Schulte-Pelkum et al., 2005; Shi et al., 2015; Xu et al., 2015; Zhang et al., 2014) (Fig. 1). The amplitudes of P- to S-waves between the Moho and the interface in the lower crust are comparable in these receiver function images, so an interface with a large S-wave velocity jump should be present in the lower crust. If there is a high- v_s layer and a sharp interface in the lower crust beneath the profile, the WARR observation in this study should result in a high- v_p layer and an abrupt interface in the lower crust in the v_p structure.

We suggest that the crust beneath the southern plateau is underplated by the high- v_p Indian lower crust in some longitude ranges (perhaps most ranges) or thickened by low- v_p intermediate granulite in other longitude ranges, such as $88 \pm 0.5^\circ\text{E}$. Our proposal receives support from new receiver function images along W-S profiles (Shi et al., 2020), which show that the RF doublet is replaced by a single converter (or a single interface) in some places, such as in the longitude range of $88 \pm 0.5^\circ\text{E}$. Shi et al. (2020) suggest that two competing processes, underthrusting and localized foundering of the Indian lower crust, are operating simultaneously on the southern plateau, with the former maintaining or increasing crustal thickness and the latter reducing crustal thickness. In the WARR observation in this study, a low- v_p lower crust on the 80-km-depth Moho supports that the crust beneath the southern plateau is thickened by felsic-intermediate granulite rather than thinned by localized foundering of Indian lower crust. The high- v_p lower crust

beneath the Tethyan Himalaya and YZS in the results also provide evidence that the Indian lower crust is terminated beneath the YZS or subducted into the upper mantle beneath the YZS in the longitude range of $88 \pm 0.5^\circ\text{E}$, which receives support from the deep seismic reflection results and the magnetotelluric results (Guo et al., 2017; Liang et al., 2018).

5.5. New geodynamic model

Based on \mathcal{E}_{HF} mapping, Hou et al. (2015) suggested that the juvenile lower crust is distributed mostly beneath the western and eastern parts of the southern Lhasa terrane but not the central part of the southern Lhasa terrane. This implies that the original lower crust has been partly destroyed or delaminated beneath the western and eastern parts of the southern Lhasa terrane, while the original lower crust beneath the central part of the southern Lhasa terrane has been retained because the eclogite transition of the lower crust has been prevented by the dominant felsic-intermediate composition.

Geochemical studies (Chung et al., 2005) show that adakites emplaced in the southern Lhasa terrane at 26-10 Ma originated from the lower part of the thickened crust by melting eclogites or garnet amphibolites. This lower crustal melting required a significantly elevated geotherm, which Chung et al. (2003) attributed of removing the thickened lithospheric mantle. The appearance of adakites, only west of 86°E and east of 89°E along the southern Lhasa terrane, supports that the thickened lithospheric mantle may include lower parts of crust removed in both the western and eastern parts but not in the central part of the southern Lhasa terrane. As a result, lithospheric thinning provides space for the underthrusting Indian lower crust beneath the western and eastern parts of the southern Lhasa terrane. The thick crust without thinning beneath the central part of the southern plateau is thick enough to stop the northward advancement of the Indian lower crust and to prevent the formation of adakites.

Based on the above discussion, we suggest that the composition of the Eurasian crust plays an important role in controlling the dip angle of the Indian subducting lithosphere (Fig. 6). If the lower crust is dominated by felsic-intermediate composition, the thickened Eurasian crust stops the northward advancement of the Indian lithosphere and results in steep subduction. In contrast, the lower crust is dominated by mafic composition, and the thickened Eurasian crust loses its lower part after eclogitization and delamination, thus providing voids for the northward advancement of the Indian lithosphere and resulting in a flat underthrust. The transition between the flat underthrust and the steep subduction of the Indian lower crust also contribute to Indian slab tearing as well as the

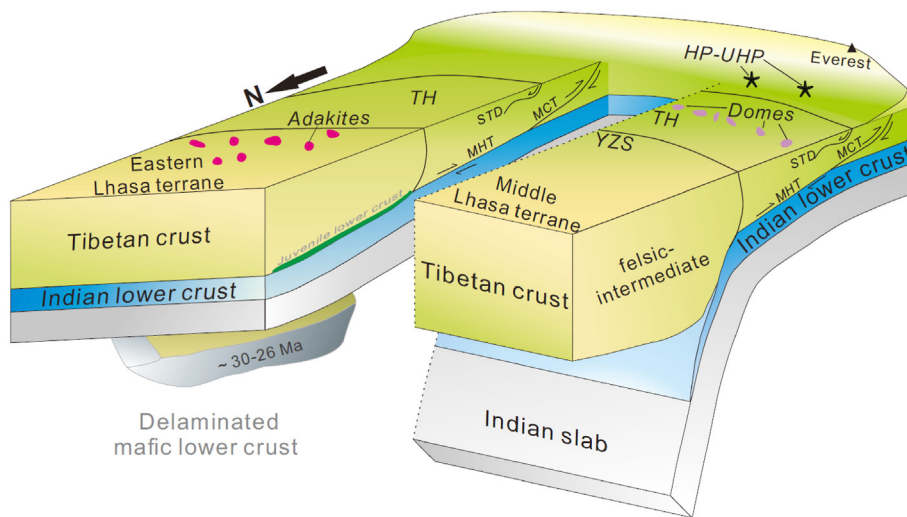


Fig. 6. Schematic model illustrating the different subduction styles of the Indian lithosphere controlled by the nature of the lower crust and thickness of the overriding plate in the southern Qinghai-Tibetan Plateau. Since ~30-26 Ma, the thickened crust in the eastern part of the Lhasa terrane has delaminated its mafic lower crust after eclogitization. It has not only caused the juvenile lower crust and the presence of adakites but has also provided space for the flat subduction of the Indian lower crust with mantle lithosphere. In the middle of the collision zone, eclogitization and further delamination due to the lack of mafic composition in the lower crust have been prevented, and the thickened crust of the southern Qinghai-Tibetan Plateau is thick enough to stop the northward advancement of the Indian lower crust, resulting in steep subduction of the Indian lithosphere. Steep subduction favors the exhumation of HP-UHP rocks, the formation of domes, and the uplift of the Mountain Everest in the middle of the collision zone.

development of N-S-trending rifts in southern Tibet and the Himalayan orogen (Chen et al., 2015; Li and Song, 2018; Zhao et al., 2010).

Along the Himalayas, HP-UHP rocks have been found only west of 80 °E and in the range of ~87–90 °E (Guillot et al., 2008; Zhang et al., 2015). Compared to the underthrust (flat subduction), the steep subduction would have space for the exhumation of HP-UHP rocks because crustal rocks can subduct to greater depth before being strongly weakened, and the two converging plates are less coupled (Li et al., 2011). We suggest that the lack of HP-UHP rocks may have resulted from underthrusting (flat subduction), although the burial and exhumation of HP-UHP rocks are also controlled by the convergence rate and rheological strength of the subducting crust. The presence of HP-UHP rocks may be an indicator of normal-angle or steep subduction of the Indian slab west of 80 °E and within ~87–90 °E.

6. Conclusions

Across the middle of the collision zone between the Indian and Eurasian plates, a new crustal v_p model is constructed beneath the Himalayas and southern Qinghai-Tibetan Plateau based on a ~450-km-long N-S-trending deep seismic sounding profile. The results show that the crustal thicknesses reach 80 km beneath the Yarlung-Zangbo Suture and southern Lhasa, decrease to 70 km under central Lhasa, and then decrease to 65 km under northern Lhasa. The Indian lower crust indicated by a v_p of ~7.1 km/s extends into the Lhasa crust no more than 50 km and perhaps subducts into the upper mantle beneath southern Lhasa. Although the burial depth is more than 50 km, the lower crust of the southern Qinghai-Tibetan Plateau features an extremely low velocity (<6.7 km/s). After comparing with the velocities of several typical crustal lithologies in different temperature regimes, this study reveals that the lower crust of the southern plateau is dominated by felsic-intermediate granulite, which prevents the lower crust from undergoing eclogitization. In the middle of the collision zone, the Eurasian crust is therefore stable and thick enough to stop the northward advancement of the Indian lithosphere and result in steep subduction. In the eastern and western parts of the collision zone, the mafic lower crust delaminated after eclogitization and gave space to the flat underthrust of the Indian lower crust.

Declaration of competing interest

The authors declare that they have no known competing financial interests or personal relationships that could have appeared to influence the work reported in this paper.

Author agreement and Acknowledgments

The authors declare that the work described was original research that has not been published previously and is not under consideration for publication elsewhere, in whole or in part. All the authors listed have approved the manuscript that is enclosed. We gratefully acknowledge our colleagues for seismic data acquisition. We thank Prof. Piotr Środa for providing the szplot software package, which was modified from the zplot of Colin A. Zelt. The software RAYINVR was provided by Zelt and Smith [1992]. The Short-period Seismograph Observation Laboratory, IGGCAS, provided the seismic instruments. This research was supported by the National Key R&D Program of China (Grant No. 2016YFC0600301) and the National Natural Science Foundation of China (Grant 42030308, 41974053, and 41888101). Most of the figures were plotted using Generic Mapping Tools (GMT) software [Wessel and Smith, 1998]. The wide-angle reflection/refraction data are shared by the Seismic Array Laboratory, IGGCAS (<https://doi.org/10.12129/IGGSL.Data.Observation>), and can be downloaded via ftp://159.226.119.161/data/DNA/88E_WA.

Appendix A. Supplementary data

Supplementary data to this article can be found online at <https://doi.org/10.1016/j.eqrea.2023.100233>.

References

- Allègre, C.J., Courtillot, V., Tapponnier, P., Hirn, A., Mattauer, M., Coulon, C., et al., 1984. Structure and evolution of the Himalaya–Tibet orogenic belt. *Nature* 307 (5946), 17–22. <https://doi.org/10.1038/307017a0>.
- Beaumont, C., Jamieson, R.A., Nguyen, M.H., Lee, B., 2001. Himalayan tectonics explained by extrusion of a low-viscosity crustal channel coupled to focused surface denudation. *Nature* 414 (6865), 738–742. <https://doi.org/10.1038/414738a>.
- Chan, G.H.N., Waters, D.J., Searle, M.P., Aitchison, J.C., Horstwood, M.S.A., Crowley, Q., et al., 2009. Probing the basement of southern Tibet: evidence from crustal xenoliths entrained in a Miocene ultrapotassic dyke. *J. Geol. Soc.* 166 (1), 45–52. <https://doi.org/10.1144/0016-76492007-145>.
- Chang, C., Chen, N., Coward, M.P., Wanning, D., Dewey, J.F., Gansser, A., et al., 1986. Preliminary conclusions of the royal society and academia sinica 1985 geotraverse of Tibet. *Nature* 323 (6088), 501–507. <https://doi.org/10.1038/323501a0>.
- Christensen, N.L., 1979. Compressional wave velocities in rocks at high temperatures and pressures, critical thermal gradients, and crustal low-velocity zones. *J. Geophys. Res.* 84 (B12), 6849–6857.
- Chen, Y., Li, W., Yuan, X., Badal, J., Teng, J., 2015. Tearing of the Indian lithospheric slab beneath southern Tibet revealed by SKS-wave splitting measurements. *Earth Planet Sci. Lett.* 413, 13–24.
- Christensen, N.L., Mooney, W.D., 1995. Seismic velocity structure and composition of the continental crust: a global view. *J. Geophys. Res.* 100 (B7), 9761–9788.

- Chung, S., Ji, J., Liu, D., Chu, M., Lee, H., Wen, D., et al., 2003. Adakites from continental collision zone: melting of thickened lower crust in southern Tibet. *Geology* 31 (11), 1021–1024.
- Chung, S., Chu, M., Zhang, Y., Xie, Y., Lo, C.H., Lee, T.Y., et al., 2005. Tibetan tectonic evolution inferred from spatial and temporal variations in post-collisional magmatism. *Earth Sci. Rev.* 68 (3), 173–196.
- Clark, M.K., Royden, L.H., 2000. Topographic ooze: building the eastern margin of Tibet by lower crustal flow. *Geology* 28 (8), 703–706.
- Coulon, C., Maluski, H., Bollinger, C., Wang, S., 1986. Mesozoic and cenozoic volcanic rocks from central and southern Tibet: ³⁹Ar–⁴⁰Ar dating, petrological characteristics and geodynamical significance. *Earth Planet Sci. Lett.* 79 (3), 281–302. [https://doi.org/10.1016/0012-821X\(86\)90186-X](https://doi.org/10.1016/0012-821X(86)90186-X).
- De Paoli, M., Clarke, G., Daczko, N., 2012. Mineral equilibria modeling of the granulite-eclogite transition: effects of whole-rock composition on metamorphic facies type-assemblages. *J. Petrol.* 53, 949–970. <https://doi.org/10.1093/ptrology/egs004>.
- Dewey, J.F., Burke, K.C.A., 1973. Tibetan, variscan, and precambrian basement reactivation: products of continental collision. *J. Geol.* 81 (6), 683–692. <https://doi.org/10.1086/627920>.
- Dong, H., Wei, W., Jin, S., Ye, G., Jones, A.G., Zhang, L., et al., 2020. Shaping the surface deformation of central and south Tibetan plateau: insights from magnetotelluric array data. *J. Geophys. Res. Solid Earth* 125 (9), e2019JB019206. <https://doi.org/10.1029/2019jb019206>.
- England, P., Houseman, G., 1986. Finite strain calculations of continental deformation: 2. Comparison with the India-Asia Collision Zone. *J. Geophys. Res.* 91 (B3), 3664–3676. <https://doi.org/10.1029/jb091ib03p03664>.
- Green, D., Ringwood, A., 1972. A comparison of recent experimental data on the gabbro-garnet granulite-eclogite transition. *J. Geol.* 80, 277–288. <https://doi.org/10.1086/627731>.
- Guillot, S., Mahéo, G., de Sigoyer, J., Hattori, K.H., Pêcher, A., 2008. Tethyan and Indian subduction viewed from the Himalayan high- to ultrahigh-pressure metamorphic rocks. *Tectonophysics* 451 (1), 225–241. <https://doi.org/10.1016/j.tecto.2007.11.059>.
- Guo, X., Gao, R., Zhao, J., Xu, X., Lu, Z., Klemperer, S.L., et al., 2018. Deep-seated lithospheric geometry in revealing collapse of the Tibetan Plateau. *Earth Sci. Res.* 185, 751–762. <https://doi.org/10.1016/j.earscires.2018.07.013>.
- Guo, X., Li, W., Gao, R., Xu, X., Li, H., Huang, X., et al., 2017. Nonuniform subduction of the Indian crust beneath the Himalayas. *Sci. Rep.* 7 (1), 12497.
- Guo, Z., Wilson, M., Zhang, M., Cheng, Z., Zhang, L., J.C.T.M and Petrology, 2013. Post-collisional, K-rich mafic magmatism in south Tibet: constraints on Indian slab-towedge transport processes and plateau uplift. *Contrib. Mineral. Petrol.* 165 (6), 1311–1340. <https://doi.org/10.1007/s00410-013-0860-y>.
- Haines, S.S., Klemperer, S.L., Brown, L., Jingru, G., Mechie, J., Meissner, R., et al., 2003. INDEPTH III seismic data: from surface observations to deep crustal processes in Tibet. *Tectonics* 22 (1), 1001. <https://doi.org/10.1029/2001TC001305>.
- Harris, N.B.W., Inger, S., Ronghua, X., 1990. Cretaceous plutonism in Central Tibet: an example of post-collision magmatism? *J. Volcanol. Geoth. Res.* 44 (1), 21–32. [https://doi.org/10.1016/0377-0273\(90\)90009-5](https://doi.org/10.1016/0377-0273(90)90009-5).
- Hole, J.A., 1992. Nonlinear high-resolution three-dimensional seismic travel time tomography. *J. Geophys. Res.* 97 (B5), 6553. <https://doi.org/10.1029/92jb00235>.
- Hou, Z., Duan, L., Lu, Y., Zheng, Y., Zhu, D., Yang, Z., et al., 2015. Lithospheric architecture of the Lhasa terrane and its control on ore deposits in the Himalayan-Tibetan orogen. *Econ. Geol.* 110, 1541–1575.
- Houseman, G., England, P., 1993. Crustal thickening versus lateral expulsion in the Indian-Asian Continental Collision. *J. Geophys. Res.* 98, 12233–12249. <https://doi.org/10.1029/93JB00443>.
- Huang, S., Yao, H., Lu, Z., Tian, X., Zheng, Y., Wang, R., et al., 2020. High-resolution 3-D shear wave velocity model of the Tibetan plateau: implications for crustal deformation and porphyry Cu deposit formation. *J. Geophys. Res. Solid Earth* 125 (7), e2019JB019215. <https://doi.org/10.1029/2019jb019215>.
- Kang, D., Zhang, Z., Palin, R.M., Tian, Z., Dong, X., 2020. Prolonged partial melting of garnet amphibolite from the eastern Himalayan syntaxis: implications for the tectonic evolution of large Hot orogens. *J. Geophys. Res. Solid Earth* 125, e2019JB019119. <https://doi.org/10.1029/2019jb019119>.
- Kapp, P., Yin, A., Harrison, T., Ding, L., 2005. Cretaceous-Tertiary shortening, basin development, and volcanism in central Tibet. *GSA Bulletin* 117, 865–878. <https://doi.org/10.1130/B25595.1>.
- Kind, R., Yuan, X., Saul, J., Nelson, D., Sobolev, S.V., Mechie, J., et al., 2002. Seismic images of crust and upper mantle beneath Tibet: evidence for Eurasian plate subduction. *Science* 298 (5596), 1219–1221. <https://doi.org/10.1126/science.1078115>.
- Lee, C.-T.A., Anderson, D.L., 2015. Continental crust formation at arcs, the arclogite “delamination” cycle, and one origin for fertile melting anomalies in the mantle. *Sci. Bull.* 60 (13), 1141–1156. <https://doi.org/10.1007/s11434-015-0828-6>.
- Li, C., Hilst, R.D.V.D., Meltzer, A.S., Engdahl, E.R., 2008. Subduction of the Indian lithosphere beneath the Tibetan Plateau and Burma. *Earth Planet Sci. Lett.* 274 (1), 157–168.
- Li, H., Gao, R., Li, W., Lu, Z., 2018. The Moho structure beneath the Yarlung Zangbo Suture and its implications: evidence from large dynamite shots. *Tectonophysics* 747–748, 390–401. <https://doi.org/10.1016/j.tecto.2018.10.003>.
- Li, J., Song, X., 2018. Tearing of Indian mantle lithosphere from high-resolution seismic images and its implications for lithosphere coupling in southern Tibet. In: *Proc. Natl. Acad. Sci. USA*, 115, pp. 8296–8300. <https://doi.org/10.1073/pnas.1717258115>, 33.
- Li, S., Unsworth, M., Booker, J., Wei, W., Handong, T., Jones, A., 2003. Partial melt or aqueous fluid in the mid-crust of Southern Tibet? Constraints from INDEPTH magnetotelluric data. *Geophys. J. Int.* 153, 289–304. <https://doi.org/10.1046/j.1365-246X.2003.01850.x>.
- Li, Z., Xu, Z., Gerya, T.V., 2011. Flat versus steep subduction: contrasting modes for the formation and exhumation of high- to ultrahigh-pressure rocks in continental collision zones. *Earth Planet Sci. Lett.* 301 (1), 65–77. <https://doi.org/10.1016/j.epsl.2010.10.014>.
- Liang, H., Jin, S., Wei, W., Gao, R., Ye, G., Zhang, L., et al., 2018. Lithospheric electrical structure of the middle Lhasa terrane in the south Tibetan plateau. *Tectonophysics* 731–732, 95–103. <https://doi.org/10.1016/j.tecto.2018.01.020>.
- Liu, H., 2003. 3D structure of the physical properties and state of the deep materials, and its forming dynamical process beneath the Tibetan plateau (No. G1998040806). In: *Research Report of National 973 Project – The Forming and Evolution of Tibetan Plateau and its Effects on Environment and Resources*.
- Liu, Q., van der Hilst, R.D., Li, Y., Yao, H., Chen, J., Guo, B., et al., 2014. Eastward expansion of the Tibetan Plateau by crustal flow and strain partitioning across faults. *Nat. Geosci.* 7 (5), 361–365. <https://doi.org/10.1038/ngeo2130>.
- Lombardo, B., Rollo, F., 2000. Two contrasting eclogite types in the Himalayas: implications for the Himalayan orogeny. *J. Geodyn.* 30 (1), 37–60. [https://doi.org/10.1016/S0264-3707\(99\)00026-5](https://doi.org/10.1016/S0264-3707(99)00026-5).
- Mitra, S., Priestley, K., Bhattacharyya, A., Gaur, V., 2005. Crustal structure and earthquake focal depths beneath northeastern India and southern Tibet. *Geophys. J. Int.* 160, 227–248. <https://doi.org/10.1111/j.1365-246X.2004.02470.x>.
- Mo, X., Hou, Z., Niu, Y., Dong, G., Qu, X., Zhao, Z., et al., 2007. Mantle contributions to crustal thickening during continental collision: evidence from Cenozoic igneous rocks in southern Tibet. *Lithos* 96 (1), 225–242. <https://doi.org/10.1016/j.lithos.2006.10.005>.
- Mo, X., Niu, Y., Dong, G., Zhao, Z., Hou, Z., Zhou, S., et al., 2008. Contribution of syn-collisional felsic magmatism to continental crust growth: a case study of the Paleogene Linzizong volcanic Succession in southern Tibet. *Chem. Geol.* 250 (1), 49–67. <https://doi.org/10.1016/j.chemgeo.2008.02.003>.
- Molnar, P., England, P., Martinod, J., 1993. Mantle dynamics, uplift of the Tibetan plateau, and the Indian monsoon. *Rev. Geophys.* 31 (4), 357–396.
- Monsalve, G., Sheehan, A., Rowe, C., Rajaure, S., 2008. Seismic structure of the crust and the upper mantle beneath the Himalayas: evidence for eclogitization of lower crustal rocks in the Indian Plate. *J. Geophys. Res.* 113, B08315. <https://doi.org/10.1029/2007jb005424>.
- Murphy, M., Yin, A., Harrison, T., Dürr, S., Chen, Z., Ryerson, F., et al., 1997. Did the Indo-Asian collision alone create the Tibetan Plateau? *Geology* 25 (8), 719–722. <https://doi.org/10.1130/0091-7613>.
- Murphy, M.A., 2007. Isotopic characteristics of the Gurla Mandhata metamorphic core complex: implications for the architecture of the Himalayan orogen. *Geology* 35 (11), 983–986. <https://doi.org/10.1130/G23774A.1>.
- Nábelek, J., Hetényi, G., Vergne, J., Sapkota, S., Kafle, B., Jiang, M., et al., 2009. Underplating in the Himalaya-Tibet collision zone revealed by the Hi-CLIMB experiment. *Science* 325 (5946), 1371–1374.
- O'Brien, P., Rötzler, J., 2003. High-pressure granulites: formation, recovery of peak conditions, and implications for tectonics. *J. Metamorph. Geol.* 21, 3–20. <https://doi.org/10.1046/j.1525-1314.2003.00420.x>.
- Owens, T.J., Zandt, G., 1997. Implications of crustal property variations for models of Tibetan plateau evolution. *Nature* 387 (6628), 37.
- Royden, L.H., Burchfiel, B.C., Rd, V.D.H., 2008. The geological evolution of the Tibetan Plateau. *Science* 321 (5892), 1054–1058.
- Rudnick, R., Fountain, D., 1995. Nature and composition of the continental-crust—a lower crustal perspective. *Rev. Geophys.* 33. <https://doi.org/10.1029/95RG01302>.
- Rudnick, R.L., 1995. Making continental crust. *Nature* 378 (6557), 571–578. <https://doi.org/10.1038/378571a0>.
- Rudnick, R.L., Gao, S., 2003. 3.01 composition of the continental crust. *Treatise on Geochemistry* 3, 1–64.
- Schärer, U., Xu, R.-H., Allègre, C.J., 1984. UPb geochronology of gangdese (Transhimalaya) plutonism in the Lhasa-Xigaze region, Tibet. *Earth Planet Sci. Lett.* 69 (2), 311–320. [https://doi.org/10.1016/0012-821X\(84\)90190-0](https://doi.org/10.1016/0012-821X(84)90190-0).
- Schulte-Pelkum, V., Monsalve, G., Sheehan, A., Pandey, M.R., Sapkota, S., Bilham, R., et al., 2005. Imaging the Indian subcontinent beneath the Himalaya. *Nature* 435 (7046), 1222–1225.
- Sheehan, A.F., de la Torre, T.L., Monsalve, G., Abers, G.A., Hacker, B.R., 2014. Physical state of Himalayan crust and uppermost mantle: constraints from seismic attenuation and velocity tomography. *J. Geophys. Res. Solid Earth* 119 (1), 567–580. <https://doi.org/10.1002/2013jb010601>.
- Shi, D., Klemperer, S.L., Shi, J., Wu, Z., Zhao, W., 2020. Localized foundering of Indian lower crust in the India-Tibet collision zone. *Proc. Natl. Acad. Sci. U.S.A.* 117 (40), 24742–24747. <https://doi.org/10.1073/pnas.2000015117>.
- Shi, D., Wu, Z., Klemperer, S.L., Zhao, W., Xue, G., Su, H., 2015. Receiver function imaging of crustal suture, steep subduction, and mantle wedge in the eastern India-Tibet continental collision zone. *Earth Planet Sci. Lett.* 414, 6–15.
- Shi, D., Zhao, W., Klemperer, S.L., Wu, Z., Mechie, J., Shi, J., et al., 2016. West-east transition from underplating to steep subduction in the India-Tibet collision zone revealed by receiver-function profiles. *Earth Planet Sci. Lett.* 452, 171–177. <https://doi.org/10.1016/j.epsl.2016.07.051>.
- Taylor, M., Yin, A., 2009. Active structures of the Himalayan-Tibetan orogen and their relationships to earthquake distribution, contemporary strain field, and Cenozoic volcanism. *Geosphere* 5 (5), 199–214.
- Teng, J., Sun, K., Xiong, S., Yao, H., Yin, Z., Chen, L., 1983. Deep seismic reflection waves and structure of the crust from dangxung to Yadong on the Xizang plateau (Tibet). *Phys. Earth Planet. In.* 31 (4), 293–306. [https://doi.org/10.1016/0031-9201\(83\)90089-4](https://doi.org/10.1016/0031-9201(83)90089-4).

- Tian, X., Chen, Y., Tseng, T.-L., Klemperer, S.L., Thybo, H., Liu, Z., et al., 2015. Weakly coupled lithospheric extension in southern Tibet. *Earth Planet Sci. Lett.* 430, 171–177.
- Unsworth, M., Jones, A., Wei, W., Marquis, G., Gokarn, S., Spratt, J., et al., 2005. Crustal rheology of the Himalaya and Southern Tibet inferred from magnetotelluric data. *Nature* 438, 78–81. <https://doi.org/10.1038/nature04154>.
- Vidale, J., 1988. Finite-difference calculation of travel times. *Bull. Seismol. Soc. Am.* 78 (6), 2062–2076.
- Vijaya Rao, V., Murty, A.S.N., Sarkar, D., Bhaskar Rao, Y.J., Khare, P., Prasad, Assrs, et al., 2015. Crustal velocity structure of the Neoproterozoic convergence zone between the eastern and western blocks of Dharwar Craton, India from seismic wide-angle studies. *Precambrian Res.* 266, 282–295. <https://doi.org/10.1016/j.precamres.2015.05.006>.
- Wang, G., Thybo, H., Artemieva, I.M., 2021. No mafic layer in 80 km thick Tibetan crust. *Nat. Commun.* 12 (1), 1069. <https://doi.org/10.1038/s41467-021-21420-z>.
- Wang, G., Wei, W., Ye, G., Jin, S., Jing, J., Zhang, L., et al., 2017. 3-D electrical structure across the Yadong-Gulu rift revealed by magnetotelluric data: new insights on the extension of the upper crust and the geometry of the underthrusting Indian lithospheric slab in southern Tibet. *Earth Planet Sci. Lett.* 474, 172–179.
- Wang, L., Pan, G., Ding, J., Yao, D., 2013. *Guidebook of 1:1,500,000 Geological Map of the Qinghai-Xizang (Tibet) Plateau and Adjacent Areas*. Geological Publishing House, Beijing, China, pp. 1–288.
- Watanabe, T., 1993. Effects of water and Melt on seismic velocity and their application to the characterization of seismic reflectors. *Geophys. Res. Lett.* 20 (24), 2933–2936. <https://doi.org/10.1029/93GL03170>.
- Wei, W., Jin, S., Ye, G., Deng, M., Jing, J., Unsworth, M., et al., 2010. Conductivity structure and rheological property of lithosphere in Southern Tibet inferred from super-broadband magnetotelluric sounding. *Sci. China Earth Sci.* 53, 189–202. <https://doi.org/10.1007/s11430-010-0001-7>.
- Wessel, P., Smith, W.H.F., 1998. New, improved version of the generic mapping Tools released. *EOS Trans. AGU* 79, 579.
- Wittlinger, G., Farra, V., Hetényi, G., Vergne, J., Nábělek, J., 2009. Seismic velocities in Southern Tibet lower crust: a receiver function approach for eclogite detection. *Geophys. J. Int.* 177 (3), 1037–1049. <https://doi.org/10.1111/j.1365-246X.2008.04084.x>.
- Xiong, S., Liu, H., 1997. Crustal structure in western Tibetan Plateau. *Chin. Sci. Bull.* 42 (8), 51–55.
- Xu, Q., Zhao, J., Yuan, X., Liu, H., Pei, S., 2015. Mapping crustal structure beneath southern Tibet: seismic evidence for continental crustal underthrusting. *Gondwana Res.* 27 (4), 1487–1493. <https://doi.org/10.1016/j.jgr.2014.01.006>.
- Xu, Q., Zhao, J., Yuan, X., Liu, H., Pei, S., 2017. Detailed configuration of the underthrusting Indian lithosphere beneath western Tibet revealed by receiver function images. *J. Geophys. Res. Solid Earth* 122 (10), 8257–8269. <https://doi.org/10.1002/2017jb014490>.
- Yang, Y., Ritzwoller, M., Zheng, Y., Shen, W., Levshin, A., Xie, Z., 2012. A synoptic view of the distribution and connectivity of the mid-crustal low velocity zone beneath Tibet. *J. Geophys. Res.* 117, B04303. <https://doi.org/10.1029/2011JB008810>.
- Yin, A., Harrison, T.M., 2000. Geologic evolution of the Himalayan-Tibetan orogen. *Annu. Rev. Earth Planet Sci.* 28 (1), 211–280.
- Yuan, X., Ni, J., Kind, R., Mechie, J., Sandvol, E., 1997. Lithospheric and upper mantle structure of southern Tibet from a seismological passive source experiment. *J. Geophys. Res.* 102 (B12), 27491–27500.
- Zelt, C.A., 1999. Modelling strategies and model assessment for wide-angle seismic traveltimes. *Geophys. J. Int.* 139 (1), 183–204. <https://doi.org/10.1046/j.1365-246X.1999.00934.x>.
- Zelt, C.A., Barton, P.J., 1998. Three-dimensional seismic refraction tomography: a comparison of two methods applied to data from the Faeroe Basin. *J. Geophys. Res.* 103 (B4), 7187–7210. <https://doi.org/10.1029/97jb03536>.
- Zelt, C.A., Smith, R.B., 1992. Seismic traveltimes inversion for 2-D crustal velocity structure. *Geophys. J. Int.* 108 (1), 16–34. <https://doi.org/10.1111/j.1365-246X.1992.tb00836.x>.
- Zhang, K., Wang, G., Ji, J., Luo, M., Kou, X., Wang, Y., et al., 2010. Paleogene-Neogene stratigraphic realm and sedimentary sequence of the Qinghai-Tibet Plateau and their response to uplift of the plateau. *Sci. China Earth Sci.* 53 (9), 1271–1294. <https://doi.org/10.1007/s11430-010-4048-2>.
- Zhang, Z., Deng, Y., Teng, J., Wang, C., Gao, R., Chen, Y., et al., 2011. An overview of the crustal structure of the Tibetan plateau after 35 years of deep seismic soundings. *J. Asian Earth Sci.* 40 (4), 977–989.
- Zhang, Z., Klemperer, S., 2010. Crustal structure of the Tethyan Himalaya, southern Tibet: new constraints from old wide-angle seismic data. *Geophys. J. Int.* 181 (3), 1247–1260. <https://doi.org/10.1111/j.1365-246X.2010.04578.x>.
- Zhang, Z., Klemperer, S.L., 2005. West-east variation in crustal thickness in northern Lhasa block, central Tibet, from deep seismic sounding data. *J. Geophys. Res.* 110. <https://doi.org/10.1029/2004JB003139>. B09403.
- Zhang, Z., Teng, J., Li, Y., Klemperer, S., Yang, L., 2004. Crustal structure of seismic velocity in southern Tibet and east-westward escape of the crustal material. *Sci. China Earth Sci.* 47 (6), 500–506.
- Zhang, Z., Wang, Y., Houseman, G.A., Xu, T., Wu, Z., Yuan, X., et al., 2014. The Moho beneath western Tibet: shear zones and eclogitization in the lower crust. *Earth Planet Sci. Lett.* 408, 370–377. <https://doi.org/10.1016/j.epsl.2014.10.022>.
- Zhang, Z., Xiang, H., Dong, X., Wangchao, L., Ding, H., Gou, Z., et al., 2015. Oligocene HP metamorphism and anatexis of the higher Himalayan crystalline sequence in Yadong region, east-central Himalaya. *Gondwana Res.* 41. <https://doi.org/10.1016/j.jgr.2015.03.002>.
- Zhao, J., Yuan, X., Liu, H., Kumar, P., Pei, S., Kind, R., et al., 2010. The boundary between the Indian and Asian tectonic plates below Tibet. *Proc. Natl. Acad. Sci. U.S.A.* 107 (25), 11229–11233.
- Zhao, L., Xie, X., He, J., Tian, X., Yao, Z., 2013. Crustal flow pattern beneath the Tibetan Plateau constrained by regional Lg-wave Q tomography. *Earth Planet Sci. Lett.* 383 (4), 113–122.
- Zhao, W., Mechie, J., Brown, L.D., Guo, J., Haines, S., Hearn, T., et al., 2001. Crustal structure of central Tibet as derived from project INDEPTH wide-angle seismic data. *Geophys. J. Int.* 145 (2), 486–498. <https://doi.org/10.1046/j.0956-540x.2001.01402.x>.
- Zhu, D., Mo, X., Niu, Y., Zhao, Z., Wang, L., Liu, Y., et al., 2009. Geochemical investigation of Early Cretaceous igneous rocks along an east–west traverse throughout the central Lhasa Terrane, Tibet. *Chem. Geol.* 268, 298–312. <https://doi.org/10.1016/j.chemgeo.2009.09.008>.
- Zhu, D., Zhao, Z., Niu, Y., Mo, X., Chung, S., Hou, Z., et al., 2011. The Lhasa Terrane: record of a microcontinent and its histories of drift and growth. *Earth Planet Sci. Lett.* 301 (1), 241–255. <https://doi.org/10.1016/j.epsl.2010.11.005>.
- Zhu, D., Wang, Q., Cawood, P.A., Zhao, Z., Mo, X., 2017. Raising the gangdese mountains in southern Tibet. *J. Geophys. Res. Solid Earth* 122 (1), 214–223.